Maximum-Likelihood Expectation-Maximization Reconstruction of Sinograms with Arbitrary Noise Distribution Using NEC-Transformations

J. Nuyts*, *Member, IEEE*, C. Michel, *Member, IEEE*, and P. Dupont

***Abstract*—The maximum-likelihood (ML) expectation-maximization (EM) [ML-EM] algorithm is being widely used for image reconstruction in positron emission tomography. The algorithm is strictly valid if the data are Poisson distributed. However, it is also often applied to processed sinograms that do not meet this requirement. This may sometimes lead to suboptimal results: streak artifacts appear and the algorithm converges toward a lower likelihood value. As a remedy, we propose two simple pixel-by-pixel methods [noise equivalent counts (NEC)-scaling and NEC-shifting] in order to transform arbitrary sinogram noise into noise which is approximately Poisson distributed (the first and second moments of the distribution match those of the Poisson distribution). The convergence speed associated with both transformation methods is compared, and the NEC-scaling method is validated with both simulations and clinical data.**

These new methods extend the ML-EM algorithm to a general purpose nonnegative reconstruction algorithm.

I. Introduction

THE maximum-likelihood (ML) expectation-maximization (EM) [ML-EM] reconstruction algorithm for emission tomography [1], [2] has a sound theoretical basis, is simple to implement and has proved to be more robust against noise and systematic inconsistencies in the data and the system matrix than filtered backprojection (FBP). As a result, it is being widely used for image reconstruction in positron emission tomography (PET) and single photon emission tomography (SPECT).

However, although the algorithm is only valid if the data are Poisson distributed, it is often applied to precorrected PET emission and even log-converted transmission sinograms. For PET emission data, random coincidence subtraction, correction for scanner sensitivity and dead time, attenuation, and scatter corrections destroy the initial Poisson distribution. Similarly, raw transmission sinograms consist of Poisson variables, but after logarithmic transformation (applied to convert the raw data to line integrals of the attenuation coefficients) the noise characteristics are very different.

Manuscript received July 27, 2000; revised December 22, 2000. This work was supported by the Flemish Fund for Scientific Research (FWO) under Grant G.0106.98. The Associate Editor responsible for coordinating the review of this paper and recommending its publication was J. A. Fessler. *Asterisk indicates corresponding author.*

*J. Nuyts is with the Department of Nuclear Medicine, K. U. Leuven, B-3000 Leuven, Belgium (e-mail: johan.nuyts@uz.kulleuven.ac.be).

C. Michel is with the PET Laboratory, Université Catholique de Louvain, B-1348 Louvain-La-Neuve, Belgium.

P. Dupont is with the Nuclear Medicine, K. U. Leuven, B-3000 Leuven, Belgium.

Publisher Item Identifier S 0278-0062(01)03552-2.

As a remedy dedicated ML algorithms have been developed to take those effects into account. The ML-EM algorithm was extended to correct for additive (e.g., random coincidences [3], [4]) and multiplicative [1] effects. Several ML-EM and ML gradient ascent algorithms were proposed for transmission tomography [1], [5], [6].

As the algorithms become more sophisticated, the implementation cost increases. For that reason, many clinical sites prefer to implement a single algorithm rather than a set of dedicated ones. As mentioned above, the choice is generally the ML-EM algorithm, often accelerated with ordered subsets (OSEM) [7]. In previous studies, it has been shown that straightforward application of the ML-EM algorithm may lead to suboptimal image quality, if the data are not Poisson distributed, both in emission [8] and in transmission tomography [9]. The most apparent effect is the appearance of streak artifacts along projection lines measured with low sensitivity, similar to those often observed in FBP reconstructions. To remedy this, we propose to transform the sinogram values to their noise equivalent counts (NEC), such that the expected variance equals the variance predicted by the Poisson model. The transformation consists of either multiplying with a scale factor or adding an offset. The reconstruction of the transformed sinogram is performed with standard ML-EM, the transformation is compensated for by introducing either a pseudosensitivity or an offset for each sinogram pixel.

In Section II, we briefly review the concept of noise equivalent count and the formulation of the ML-EM algorithm, and show how NEC-transformations can extend the scope of the algorithm to data with statistics different from the Poisson distribution. The convergence speed associated with both NEC-transformations is compared. Section III describes two simulations which were performed to validate the method: a contaminated emission and a transmission measurement. It also describes an implementation of the NEC-scaling method for clinical whole body transmission data. The last two sections describe and discuss the results obtained from the simulations and from the clinical study.

II. Theory

A. Noise Equivalent Counts and NEC-Transformations

Because the variance of a Poisson distribution equals its mean, the mean value of a Poisson variable equals the square of its signal-to-noise ratio (SNR). As a result, it is common practice to compare measured counts directly to assess differences in SNR. However, when Poisson data are processed, the

noise characteristics are affected and the resulting values are no longer good estimates of the squared SNR. To solve this, any non Poisson value can be transformed to its so-called noise equivalent count [10]. By definition, the NEC of x is the mean of the Poisson distribution with the same SNR as x. It follows that the NEC equals the square of the SNR. Thus, Poisson variables can be directly compared to the NEC's of non Poisson variables to evaluate differences in SNR.

The transformation to NEC is not unique. Here, we consider either scaling or shifting the distribution. For NEC scaling, a scale factor a is introduced, defined by

$$\text{variance}(ax) = a\,\text{mean}(x) \tag{1}$$

where x is the variable to be transformed. Since $\text{variance}(ax) = a^2\text{variance}(x)$, the scale factor equals

$$a = \frac{\text{mean}(x)}{\text{variance}(x)}. \tag{2}$$

For NEC-shift, an offset g is introduced, defined by

$$\text{variance}(x+g) = \text{mean}(x+g). \tag{3}$$

Since $\text{variance}(g) = 0$ and $\text{mean}(g) = g$, the offset equals

$$g = \text{variance}(x) - \text{mean}(x). \tag{4}$$

By definition, the NEC-scale factor equals one and the NEC-shift equals zero if x is a Poisson variable. Note that the probability distribution of a NEC-variable has the same variance, but not necessarily the same shape as the corresponding Poisson distribution.

B. The ML-EM Algorithm

The ML-EM-algorithm [1], [2] is designed to compute the most likely distribution $\vec{\lambda}$ from the measurements $\vec{y}$, under the assumption that the values y_i of $\vec{y}$ are Poisson distributed with mean value $\sum_j c_{ij}\lambda_j$, where c_{ij} is the probability that an event (photon or pair of photons) emitted at pixel j is detected at detection bin i. The ML-EM algorithm can be written as [1]

$$\lambda_j^{\text{new}} = \frac{\lambda_j}{\sum_i c_{ij}} \sum_i c_{ij} \frac{y_i}{\sum_k c_{ik}\lambda_k}. \tag{5}$$

If the detection probability c_{ij} contains a contribution α_i independent from j, one can factorize c_{ij} as $\alpha_i v_{ij}$

$$\begin{aligned}\lambda_j^{\text{new}} &= \frac{\lambda_j}{\sum_i \alpha_i v_{ij}} \sum_i \alpha_i v_{ij} \frac{y_i}{\alpha_i \sum_k v_{ik}\lambda_k} \\ &= \frac{\lambda_j}{\sum_i \alpha_i v_{ij}} \sum_i v_{ij} \frac{y_i}{\sum_k v_{ik}\lambda_k}.\end{aligned} \tag{6}$$

Equation (6) shows that the ML-EM algorithm compares the raw counts y_i to the computed values $\alpha_i \sum_k v_{ik}\lambda_k$. The ratios are backprojected to pixel j by computing the average over all detectors i, weighted with the detection probabilities $\alpha_i v_{ij}$. The factors α_i cancel out except in the normalizing image $\sum_i \alpha_i v_{ij}$ [see (6)]. Since α_i is independent of position j, it is usually regarded as a detection sensitivity.

When the statistics of the data differ from the Poisson distribution, the EM strategy can still be applied, but leads to an algorithm different from (5). To avoid the need for a set of dedicated algorithms, we propose to transform the data into samples from a distribution which closely resembles the Poisson distribution, such that the ML-EM algorithm (5) can be applied.

C. NEC-Scaling

Only the first two moments of a NEC transformed distribution correspond to those of a Poisson distribution. We hypothesize that this approximation is sufficiently accurate to preserve all desirable properties of the ML-EM algorithm applied to pure Poisson data. ML-EM reconstruction from a NEC-scaled sinogram is accomplished by setting

$$\begin{aligned} y_i &= a_i x_i \\ \alpha_i &= a_i. \end{aligned} \tag{7}$$

in (6), where $\{x_i, i = 1 \ldots I\}$ is the non Poisson distributed sinogram and a_i is given by (2). Indeed, the transformed sinogram values $a_i x_i$ are approximately Poisson distributed as required, and the algorithm compensates for the undesired scale factor a_i by treating it as a pseudosensitivity.

To reconstruct sinograms when an estimate of the variance is available, one could use a weighted least squares algorithm, as proposed by Fessler [11]. ML-EM reconstruction after NEC scaling optimizes a very similar objective function: both methods use the same variance, the only difference is that weighted least squares assumes a Gaussian distribution, whereas the NEC-scaled ML-EM method assumes a Poisson distribution. It is well known that both distributions are very similar except for very low counts. In general, the true distribution of processed sinogram values is often neither Gaussian nor Poisson.

A consequence of the Poisson model is that NEC-scaled ML-EM always produces nonnegative reconstruction images (which is usually an advantage), and cannot process negative detection values (which is a limitation). Consequently, negative sinogram values must be eliminated, e.g., by setting them to zero.

It is easy to verify that for a multiplicative precorrection of Poisson data, e.g., precorrection for attenuation and normalization in PET, NEC scaling produces the correct ML-EM algorithm (6) (which was called "attenuation and normalization weighted ML-EM" in [8]).

D. NEC-Shift

Mean and variance can also be transformed into those of a Poisson distribution by using a pixel-dependent term instead of a pixel-dependent factor. This NEC-shift method is based on the extension of the ML-EM algorithm compensating for an additive contribution with known mean, e.g., a scatter term. Assuming that the observed measurement is a Poisson realization with mean value $\sum_j c_{ij}\lambda_j + \gamma_i$ with unknown $\vec{\lambda}$ and known $\vec{\gamma}$, the ML-EM algorithm becomes

$$\lambda_j^{\text{new}} = \frac{\lambda_j}{\sum_i c_{ij}} \sum_i c_{ij} \frac{y_i}{\sum_k c_{ik}\lambda_k + \gamma_i}. \tag{8}$$

The NEC-shifted data can be reconstructed with (8) by setting

$$y_i = x_i + g_i$$
$$\gamma_i = g_i = \text{variance}(x_i) - \text{mean}(x_i). \tag{9}$$

In contrast to NEC scaling, NEC-shift can handle negative pixel values x_i, provided that the transformed value y_i is nonnegative. An interesting example is the application of NEC-shift to randoms precorrection in PET. Assuming that q_i is the prompt coincidence count and r_i is an independent (Poisson distributed) estimate of the randoms contribution in q_i, we obtain

$$x_i = q_i - r_i$$
$$g_i = \text{variance}(x_i) - \text{mean}(x_i) = 2r_i \tag{10}$$

where we have used the Poisson variables as estimates for their mean. This is the shifted Poisson method proposed by Yavuz *et al.* in [4].

E. Convergence Speed

To compare the convergence speed of NEC-scaled ML-EM with that of NEC-shifted ML-EM, we compute the additive updates for a single iteration near the solution. The update terms can be compared by computing the NEC-shift offset as a function of the NEC-scale factor. If NEC scaling and NEC-shift are applied to the same problem, combining (2) and (9) yields

$$g_i = \text{mean}(x_i)\frac{1-a_i}{a_i}. \tag{11}$$

ML-EM with NEC scaling can be rewritten in an additive way, combining (6) and (7)

$$\lambda_j^{\text{new}} = \frac{\lambda_j}{\sum_i a_i v_{ij}} \sum_i a_i v_{ij} \frac{x_i}{\sum_k v_{ik}\lambda_k} \tag{12}$$
$$= \lambda_j + \frac{\lambda_j}{\sum_i a_i v_{ij}} \sum_i a_i v_{ij} \frac{x_i - \sum_k v_{ik}\lambda_k}{\sum_k v_{ik}\lambda_k} \tag{13}$$

Similarly, for NEC-shift, by combining (8) and (9) and accounting for the fact that $c_{ij} = v_{ij}$ (because there is no scaling in NEC-shift), we obtain

$$\lambda_j^{\text{new}} = \lambda_j + \frac{\lambda_j}{\sum_i v_{ij}} \sum_i v_{ij} \frac{x_i - \sum_k v_{ik}\lambda_k}{\sum_k v_{ik}\lambda_k + g_i}. \tag{14}$$

Inserting (11) and replacing $\text{mean}(x_i)$ with $\sum_k v_{ik}\lambda_k$, which is a good approximation near the solution, yields

$$\lambda_j^{\text{new}} \simeq \lambda_j + \frac{\lambda_j}{\sum_i v_{ij}} \sum_i a_i v_{ij} \frac{x_i - \sum_k v_{ik}\lambda_k}{\sum_k v_{ik}\lambda_k}. \tag{15}$$

It follows that for $a_i < 1$ and $g_i > 0$, NEC scaling leads to a larger step per iteration as compared to NEC-shift. The effect on convergence is complex, but since ML-EM tends to converge slowly and can be accelerated with overrelaxation [12], one would expect that decreasing the step size should slow down convergence. If $a_i > 1$ and $g_i < 0$, the NEC-shift reconstruction uses a larger step size. However, in extreme cases, the denominator in (14) may get close to zero or even become negative during iterations, leading to numerical problems [the derivation of (8) assumes that the offset is nonnegative]. In contrast, ML-EM with NEC scaling still converges when $a_i > 1$. As can be seen in (12), the algorithm is not affected if all a_i are multiplied with a constant, so one can always normalize the values to a physically meaningful range.

F. General NEC-Method

A more general transformation, combining scaling and shifting, may be proposed to optimize convergence speed while avoiding bias due to zero thresholding negative values. Recall that for NEC scaling negative sinogram values must be set to zero, which may introduce positive bias in the reconstructed images. This problem can be avoided by using an appropriate shift. Requiring $\text{variance}(a_i(x_i + g_i)) = \text{mean}(a_i(x_i + g_i))$ with $x_i + g_i > 0$ results in

$$a_i = \frac{\text{mean}(x_i) + g_i}{\text{variance}(x_i)} \tag{16}$$

where g_i is a function designed to ensure that $x_i + g_i > 0$. The presence of a_i and g_i is compensated for by setting $y_i = a_i x_i + a_i g_i, \alpha_i = a_i$ and $\gamma_i = a_i g_i$ in (8), with $c_{ij} = \alpha_i v_{ij}$. Convergence is guaranteed since $a_i g_i \geq 0$, and convergence speed can be optimized by keeping g_i small.

In the remainder of this paper, we have assumed that negative values are rare and can be set to zero without damage, such that simple NEC scaling can be applied. The focus is on NEC scaling, but for comparison the NEC-shift method (shifted Poisson model) has been applied for the contaminated emission experiment described below.

G. Applications

NEC scaling has been evaluated in two applications: a contaminated emission sinogram and a processed PET transmission scan.

1) Emission Tomography: Assume that the observed counts $\vec{s}$ are corrupted by an unknown contribution, for which an estimate $\vec{r}$ is available. Assume also that $\vec{s}$ and $\vec{r}$ are samples from a Poisson distribution. The precorrected sinogram (estimating the uncontaminated counts) equals $\vec{x} = \vec{s} - \vec{r}$. The sinogram of NEC-scale factors $\vec{a}$ has elements

$$a_i = \frac{\text{mean}(x_i)}{\text{variance}(x_i)}. \tag{17}$$

Both the mean and variance are unknown, but estimates can be obtained from the observed values s_i and r_i. For most applications, it is reasonable to assume that neighboring pixels tend to have similar means, so smoothing the raw data should yield useful estimates for mean and variance

$$\vec{a} = \frac{\text{mean}(\vec{x})}{\text{variance}(\vec{x})} \simeq \frac{\vec{G} \otimes \vec{x}}{\vec{G} \otimes (\vec{s} + \vec{r})} \tag{18}$$

where $\otimes$ denotes convolution, $\vec{G}$ is a Gaussian smoothing mask and division is executed on a pixel-by-pixel basis. Note that smoothing is only applied for estimating the NEC-scale factors a_i, we do not smooth the precorrected values x_i prior to ML-EM reconstruction. We used a mask with FWHM of two pixels, we have not investigated the effect of using different smoothing masks. A problem with (18) is that a_i approaches zero when

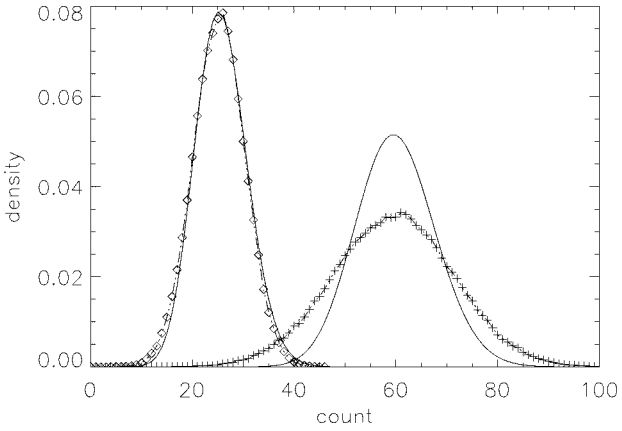

Fig. 1. NEC scaling for contaminated emission scan. A mean emission activity of 60 counts was corrupted by a contaminator with mean of 100 counts. 10^5 samples have been computed for the observed count and the contamination estimate. The distribution of the precorrected counts $(+)$ differs markedly from the Poisson distribution with the same mean (solid line). After NEC scaling ($a = 0.375$), the scaled counts (diamonds) are nearly Poisson distributed (solid line).

x_i approaches zero. This implies a zero weight for most projection lines outside the object, resulting in a poor reconstruction of the background and corresponding bias in the object. To prevent this, it suffices to threshold $\vec{x}$ at a small value ϵ in the computation of $\vec{a}$: $\vec{a} = (\vec{G} \otimes \max[\vec{x}, \epsilon])/(\vec{G} \otimes (\vec{s} + \vec{r}))$. Fig. 1 compares the histogram of a precorrected distribution and its NEC-scaled version to the Poisson distributions with the same mean.

2) Transmission Tomography: Assume that the observed counts $\vec{t}$ are Poisson distributed with mean value given by

$$\text{mean}(t_i) = b_i e^{-\sum_j l_{ij}\mu_j} \tag{19}$$

with known b_i and unknown μ_j, and with l_{ij} the effective intersection length of pixel j with projection line i. The processed transmission sinogram $\vec{x}$ is computed as

$$x_i = \ln\left(\frac{b_i}{t_i}\right). \tag{20}$$

The variance is estimated as

$$\text{variance}(x_i) \simeq \left(\frac{\partial x_i}{\partial t_i}\right)^2 \times \text{variance}(t_i) = \frac{1}{\text{mean}(t_i)}. \tag{21}$$

Again, the mean values and variances are not exactly known. One can estimate the scale factors as

$$\vec{a} = \vec{G} \otimes (\max[\vec{x}, \epsilon] \times \vec{t}). \tag{22}$$

where $\vec{G}$ is the same kernel as in (18) and $\times$ denotes pixel-by-pixel multiplication. Thresholding to a small positive value ϵ is applied to prevent zero weights for projection lines not intersecting the object, as in (18). We used $\epsilon = 0.1$. Fig. 2 compares the histograms of a processed transmission value before and after NEC scaling.

Note that the log conversion is a nonlinear operator, which causes positive bias in the presence of noise. In practice, the noise, and hence the bias, are often reduced by presmoothing $\vec{b}$ and $\vec{t}$ in (20) when reconstructing from processed transmission scans.

III. Experiments

The method has been validated on simulations and on whole body transmission measurements for a clinical study. We simulated an emission scan $\vec{s}$ contaminated by an additional source, for which a noisy estimate $\vec{r}$ was available. Possible sources of such a contamination are residual activity from a previous scan, fiducial markers, or random and scatter coincidences. We considered a strong contamination so that the artifacts are more obvious. We also simulated a transmission protocol.

For the simulations, Poisson realizations have been computed using the method suggested in [13]: for mean values smaller than 12, exponential deviates are simulated, for larger values smaller than 50, the rejection method is applied. In both cases, the uniform pseudorandom generator from IDL (Research Systems, Inc, Boulder CO) was used. For values exceeding 50, Poisson noise was approximated as Gaussian noise, normally distributed values were computed with IDL's Gaussian pseudorandom generator. The simulations focused on the noise properties, assuming an idealized detection system and no scatter.

Finally, the NEC-scaling method was implemented to reconstruct attenuation images from clinical PET data using a 3-min and 10-min transmission scan.

A. Simulated Contaminated Emission Scan

Unattenuated and noise-free emission projections were computed from a phantom consisting of ellipses, simulating a radioactive object. The resulting noise-free sinogram consisted of 100 detectors and 100 projection angles. The contamination source was a smaller circular object; its projections were calculated separately and stored in a second sinogram. To simulate a measured contaminated sinogram $\vec{s}$, both sinograms were added and used as the mean value to compute a Poisson realization. To simulate a measured estimate $\vec{r}$ of the contaminating source, an independent Poisson realization was computed from the second noise-free sinogram. There were 1.6×10^7 counts in $\vec{s}$ and 1.1×10^7 in $\vec{r}$. Fig. 3 shows the image without and with contaminating source.

The task is to reconstruct an emission image unaffected by the contaminating source. For that purpose, the simulated measurement was precorrected by subtracting the contamination estimate: $\vec{x} = \vec{s} - \vec{r}$. The precorrected sinogram $\vec{x}$ was reconstructed with FBP (ramp filter, cutoff at Nyquist frequency), unweighted ML-EM [UW ML-EM, straightforward application of (5)], NEC-scaled ML-EM [(6) with (18)], and NEC-shifted ML-EM [(8) with (9)].

B. Simulated Transmission Protocol

A noise-free transmission sinogram from a phantom consisting of ellipses was computed using (19), with $b_i = 250$. The mean transmission count was 60. Poisson noise was added, and the projection of the attenuation coefficients was obtained by using (20).

The transformed sinogram was reconstructed with UW ML-EM and with NEC-scaled ML-EM using (22). In addition, the raw data $(\vec{t}, \vec{b})$ were reconstructed with an ML-gradient ascent algorithm dedicated to transmission tomography [9],

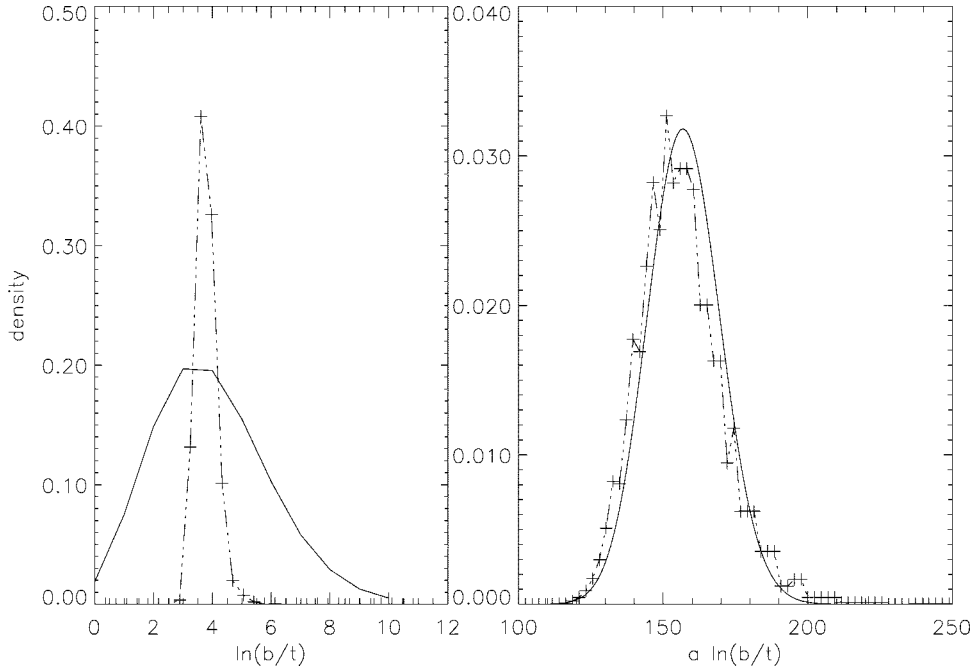

(a) (b)

Fig. 2. NEC scaling for processed transmission scan. Blank count was 500 and noise free, mean transmission count was 10 and 10^5 samples were simulated. (a) Original histogram of log-converted values $(+)$ and Poisson distribution with same mean. (b) Histogram $(+)$ after NEC scaling ($a = 39.64$) and corresponding Poisson distribution.

(a) (b)

Fig. 3. Simulation of contaminated emission scan. (a) The undisturbed activity distribution. (b) Activity distribution in the presence of the contaminating source.

[14], which will be called "MLTR" hereafter. This method assumes that $\vec{t}$ is a Poisson realization and $\vec{b}$ is noise-free. Since these assumptions are correct for this simulation, MLTR can be regarded as the reference method. NEC-shifted ML-EM did not converge because many offsets g_i were negative [see (9)], causing numerical problems as explained in Section II-E.

C. Patient Transmission Protocol

PET whole body transmission data were acquired on an ECAT EXACT HR (CTI, Knoxville, TN), the characteristics of which have been described previously [15]. This whole body high-resolution tomograph allows simultaneous imaging of 47 transaxial slices (3.125-mm thickness) in a 15 cm axial field-of-view. In two-dimensional (2-D) acquisition mode (septa extended, ring difference five, span 11), the nominal in-plane resolution is around 5-mm full-width-at-half-maximum (FWHM) and the axial resolution is around 4 mm at field-of-view center.

Transmission data were acquired in 2-D and true (i.e., prompt-delayed) coincidence mode using three rotating ^{68}Ge rod sources (total activity around 180 MBq) and a seven-bin-wide rod mask [16]. A long blank scan (60 million true events, 65 min) was first acquired and was followed by transmission scans at three bed positions on the chest of a heavy volunteer. Acquisition time was set to 3 min to reproduce usual acquisition conditions of a whole body protocol [17]. Another 10-min transmission scan was also performed for comparison. The overlap between contiguous bed positions was seven slices (2.5 cm) in order to achieve a quasi-uniform axial sensitivity.

Blank and transmission data were corrected for 2-D-normalization (including dead-time) and scanner curvature. Transmission data were considered to be scatter-free. Whole body projections were assembled with bed position overlap for both transmission and blank scans and smoothed with an arbitrary 8-mm FWHM 2-D Gaussian kernel. They provided the standard attenuation (A_{std}) as the ratio of smoothed blank over smoothed transmission. The attenuation image was reconstructed from $\ln(A_{\mathrm{std}})$ using either FBP (ramp filter, cutoff at Nyquist frequency), UW OSEM, or NEC-weighted OSEM. In the latter case, since the blank scan measurement is arbitrarily long, we assumed that it was noise-free. The NEC-scale sinogram was obtained using (22) as explained in Section II-G2. Both UW and NEC-weighted OSEM reconstructions were stopped after six iterations with 14 subsets (roughly equivalent to 84 NEC-scaled ML-EM iterations). No post-smoothing was applied to the images.

For comparison, the raw blank, transmission and normalization data have also been reconstructed with the MLTR program. No priors were used, and a scheme with decreasing number of subsets was applied: two iterations of 28 subsets, followed

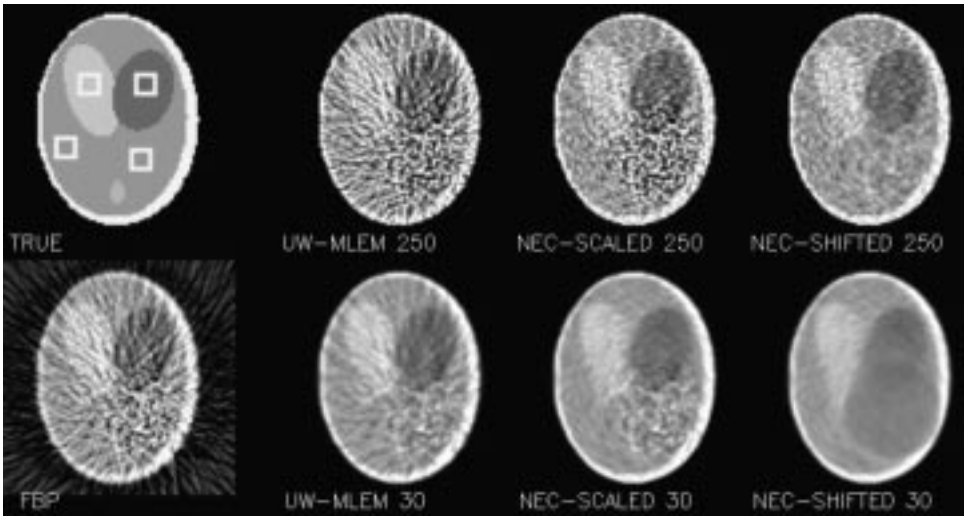

Fig. 4. Simulation of contaminated emission scan. Top row, from left to right: true phantom image; UW ML-EM, NEC-scaled ML-EM, and NEC-shifted ML-EM at 250 iterations. Bottom row: FBP (ramp filter with cutoff at Nyquist frequency); UW ML-EM, NEC-scaled ML-EM, and NEC-shifted ML-EM at 30 iterations. Four regions are shown in overlay on the true image (numbered from 1 to 4, clockwise starting upper left).

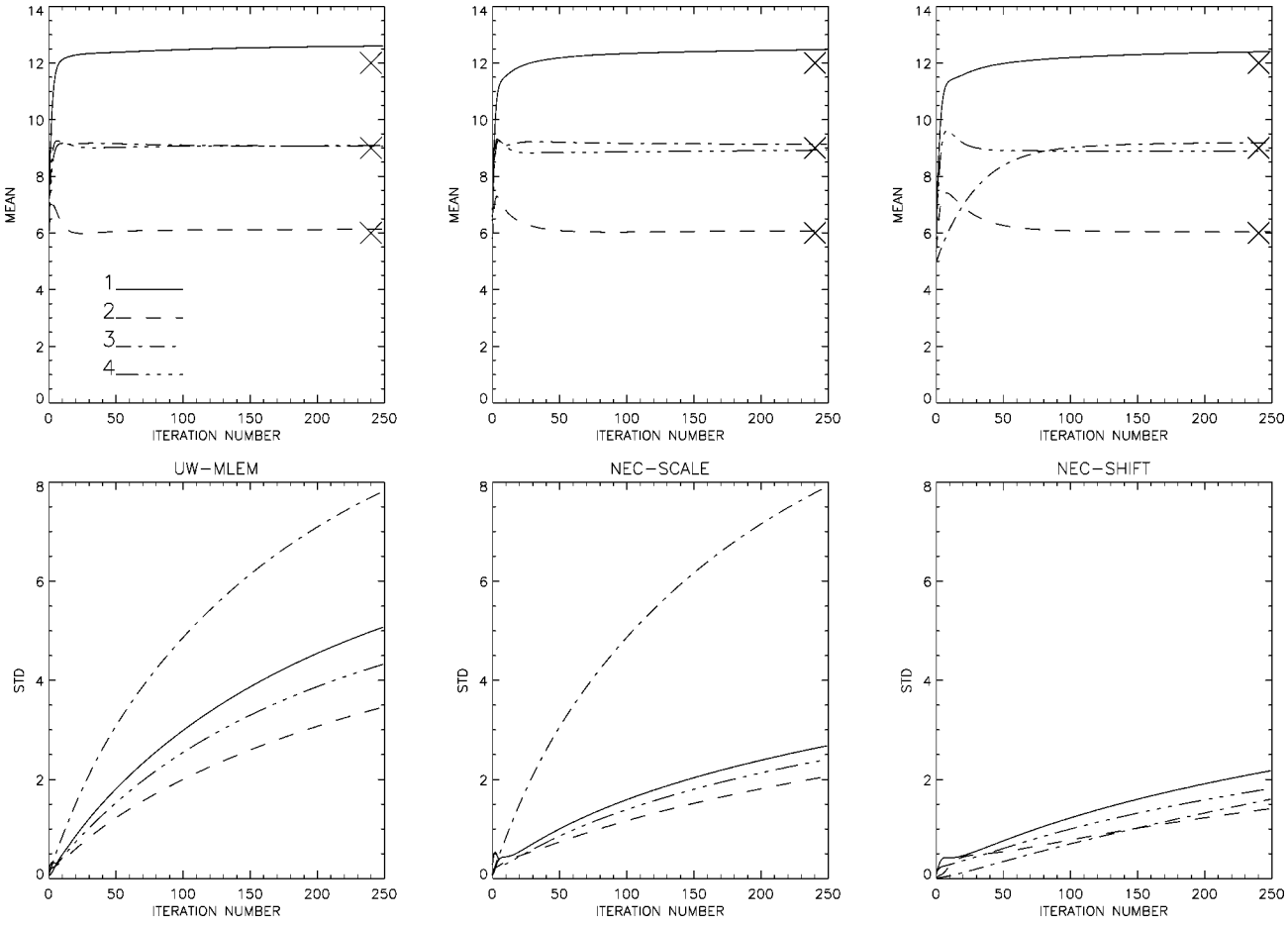

Fig. 5. Contaminated emission scan: region mean and standard deviations as a function of iteration number, for each of the iterative algorithms. The four regions are shown in Fig. 4, they are numbered in clockwise direction, starting with the most active region (region 3 is in the center of the contaminated area). The true region values are indicated with the symbol X. Top row shows mean values, bottom row standard deviations. From left to right: UW ML-EM; NEC-scaled-ML-EM; and NEC-shifted ML-EM.

by one of 14, one of seven, and one of four subsets, which is roughly equivalent to 81 nonaccelerated iterations.

In order to detect possible bias, the mean values in several tissue regions and in the lungs have been compared.

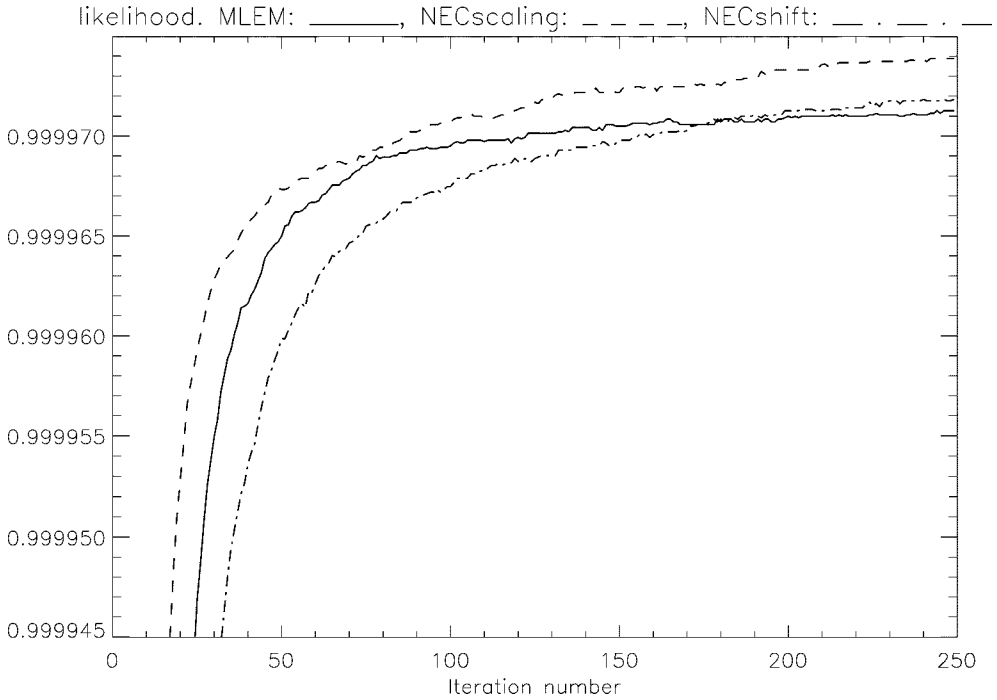

Fig. 6. Normalized log likelihood for simulated contaminated emission scan as a function of the iteration number. Solid line: UW ML-EM; dashed line: NEC-scaled-ML-EM; and dash-dotted line: NEC-shifted ML-EM.

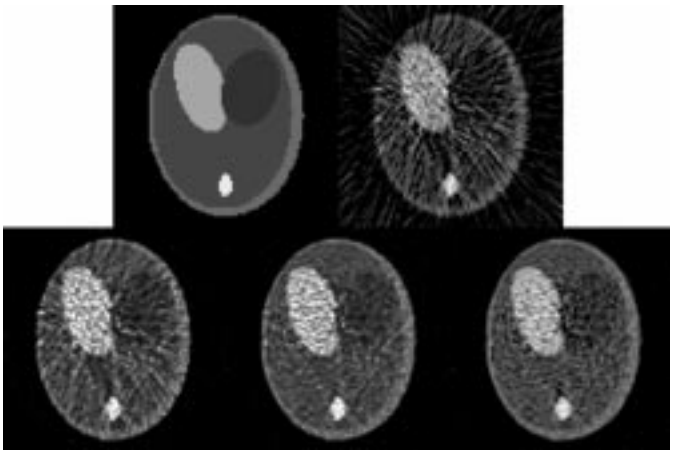

Fig. 7. Simulated transmission scan. Top row: true image and FBP. Bottom row: UW ML-EM, NEC-scaled ML-EM, and MLTR; all at 100 iterations.

IV. Results

A. Simulated Contaminated Emission Scan

Fig. 4 shows the UW ML-EM, NEC-scaled ML-EM, and NEC-shifted ML-EM images after 30 and 250 iterations, together with the true image and with FBP. Both the FBP and UW ML-EM images show streak artifacts, which tend to be oriented toward the contaminated region. In contrast, there are no streak artifacts in the NEC ML-EM reconstructions. The NEC-scaled ML-EM image is noisier in the contaminated region than in the rest of the image, due to additional noise from the contaminating object. The NEC-shifted ML-EM image converges slower, in particular in the contaminated region, as predicted by (15): at early iterations, the contaminated region is nearly homogenous, at higher iterations noise increases as in the NEC-scaled ML-EM image. The mean and standard deviation of the four regions indicated in Fig. 4 are plotted in Fig. 5, clearly demonstrating the position-dependent differences in convergence speed. Note that the plots are for a single noise realization, showing the combined effect of noise and possible bias. All methods were unbiased in absence of noise (data not shown).

The likelihood of the projections, given the reconstruction and the contamination sinogram, equals [1]

$$p(\vec{y}\,|\,\vec{\lambda}) = \prod_i e^{-\left(\sum_j c_{ij}\lambda_j + \bar{c}_i\right)} \frac{\left(\sum_j c_{ij}\lambda_j + \bar{c}_i\right)^{s_i}}{s_i!} \tag{23}$$

where

- s_i "measured" sinogram value;
- λ_j current reconstruction;
- c_{ij} detection probabilities;
- $\bar{c}_i$ noise-free contaminating sinogram (which is available in this simulation, but not in a real application).

Fig. 6 compares the normalized log-likelihood as a function of the iteration number for the three iterative algorithms. This value was computed by taking the logarithm of (23), dropping terms independent of $\vec{\lambda}$ and dividing by the upper limit, reached when computed and measured sinograms are identical

$$\frac{\sum_i \left[s_i \ln\left(\sum_j c_{ij}\lambda_j + \bar{c}_i\right) - \left(\sum_j c_{ij}\lambda_j + \bar{c}_i\right)\right]}{\sum_i [s_i \ln s_i - s_i]}. \tag{24}$$

B. Simulated Transmission Protocol

Fig. 7 shows the true attenuation image and the reconstruction from its noisy projections obtained with FBP and with UW ML-EM, NEC-scaled ML-EM, and MLTR at 100 iterations.

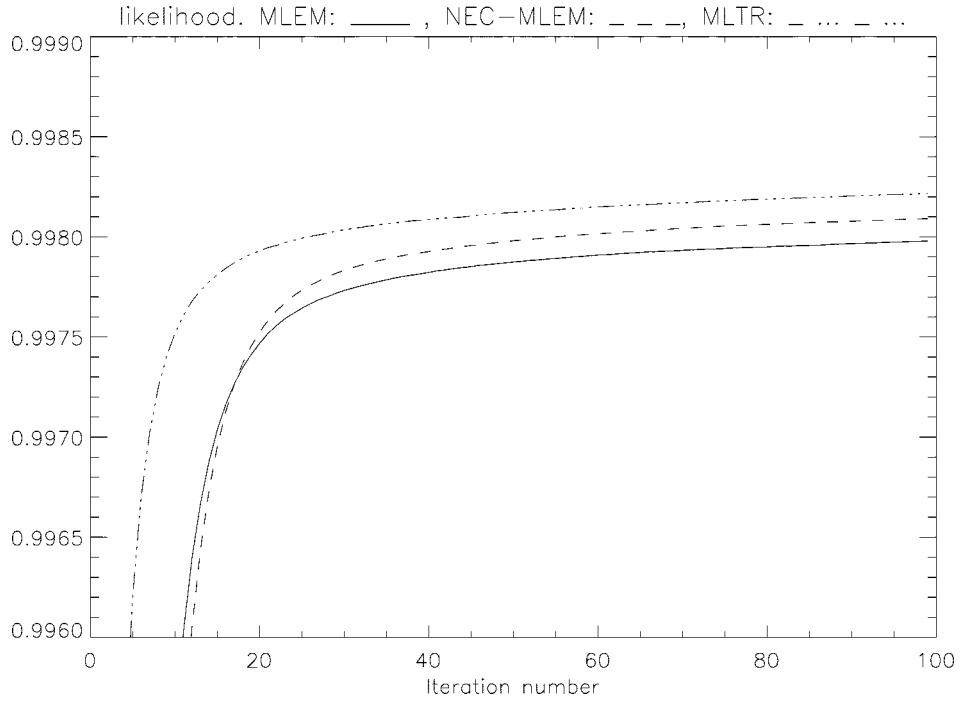

Fig. 8. Normalized log-likelihood for the simulated transmission scan as a function of the iteration number. Solid line: UW ML-EM; dashed line: NEC-scaled ML-EM; and dash-dotted line: MLTR.

Fig. 8 plots the normalized log-likelihood of the three iterative reconstruction methods as a function of the iteration number. The log-likelihood was computed as

$$\frac{\sum_i \left[t_i \ln\left(b_i \exp\left(-\sum_j l_{ij}\mu_j\right)\right) - b_i \exp\left(-\sum_j l_{ij}\mu_j\right)\right]}{\sum_i [t_i \ln t_i - t_i]} \tag{25}$$

where

- t_i "measured" transmission value;
- b_i blank value;
- l_{ij} intersection length of line i with pixel j;
- μ_j current reconstruction value [1].

C. Patient Transmission Scan

Fig. 9 shows seven transaxial slices reconstructed from the short transmission scan with the four reconstruction algorithms. The slices were selected because of obvious streak artifacts in the FBP images. These artifacts are still present in the UW ML-EM reconstruction, but disappear when NEC scaling is applied. Fig. 10 shows the same reconstructed slices for the long transmission scan.

On each of the seven planes, an elliptical region was drawn manually. The regions are shown in overlay in Figs. 9 and 10. In Fig. 11, the mean values of the regions have been plotted for the four reconstruction methods and the two transmission scans. Region 5 was selected in the lung to examine the useful dynamic range in a transmission experiment. The region values were similar for all methods. A paired t-test comparing the 14 region values did not reveal a significant difference between NEC and any other method ($p = 0.54$ or higher). Similarly, a paired t-test found no significant difference between the region values obtained with NEC-scaled ML-EM from the short versus the long transmission scan ($p = 0.4$).

V. Discussion

Unless some constraining is applied, reconstruction algorithms estimate, for every pixel, the actual number of emitted photons that have been detected during the acquisition, rather than the mean of the corresponding distribution. Consequently, if the number of detected events is relatively low, the reconstructed image is always noisy. However, since radioactive decay is an independent process, the noise in the reconstructed image should be uncorrelated. Strongly correlated noise, such as streak artifacts, should only appear if the reconstruction algorithm is not a sufficiently accurate inverse of the acquisition process. Avoiding correlated noise is particularly important when the likelihood is combined with a smoothing prior, since the prior is effective against pixel noise but not against streaks or other artifacts with strong spatial correlation. The proposed NEC-algorithms are efficient methods to minimize correlated noise.

Our experiments show that UW ML-EM reconstruction of non Poisson distributed data may cause such streak artifacts. NEC scaling approximately restores the Poisson distribution, and therefore improves the correspondence between the mathematical model (Poisson statistics) and the true characteristics of the data. This results in reduction of correlated noise such as streak artifacts. In contrast, the uncorrelated reconstruction noise (or more precisely: noise only exhibiting significant correlations over very short distances) is a direct consequence of the uncertainty in the data. We have not examined the effect of

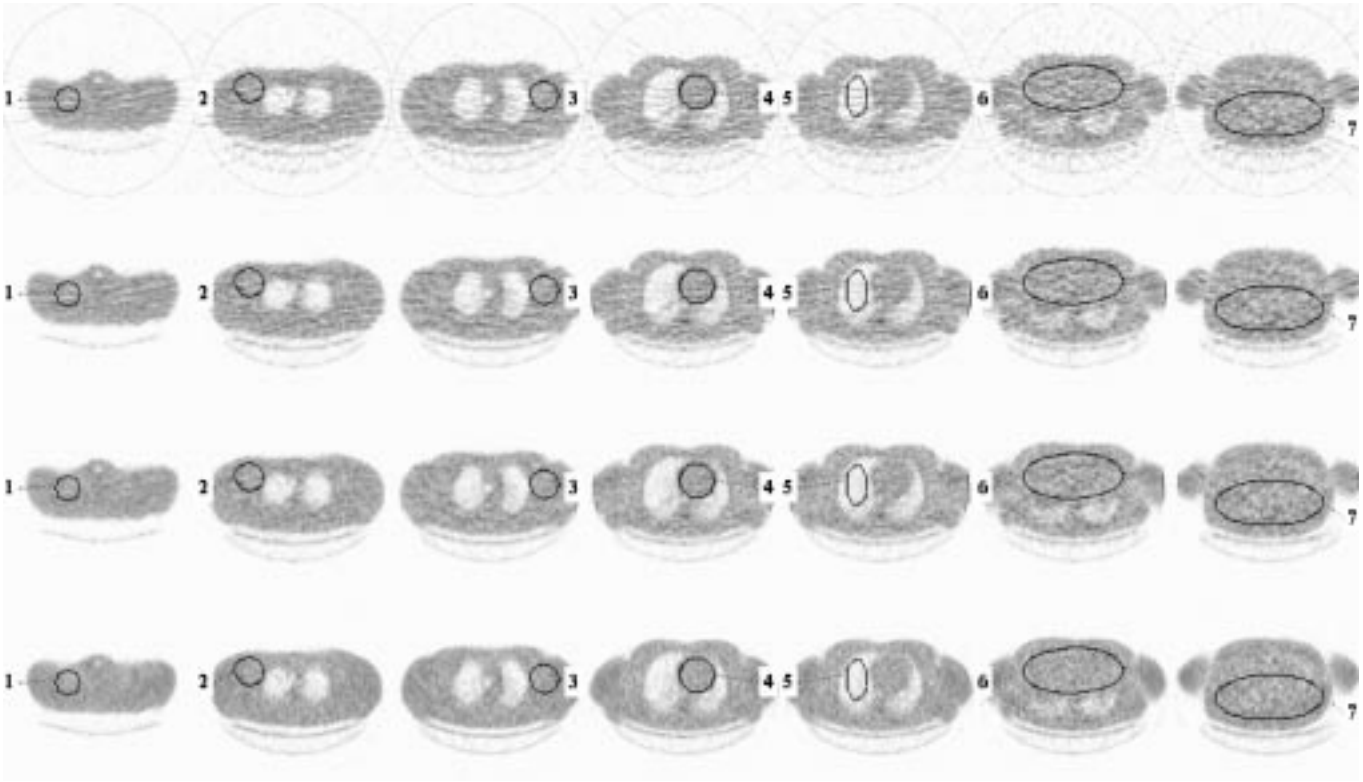

Fig. 9. Reconstruction images from the 3-min transmission scan. From top to bottom: FBP; UW ML-EM; NEC-scaled ML-EM; and MLTR. For each algorithm, seven planes are shown with the seven regions in overlay.

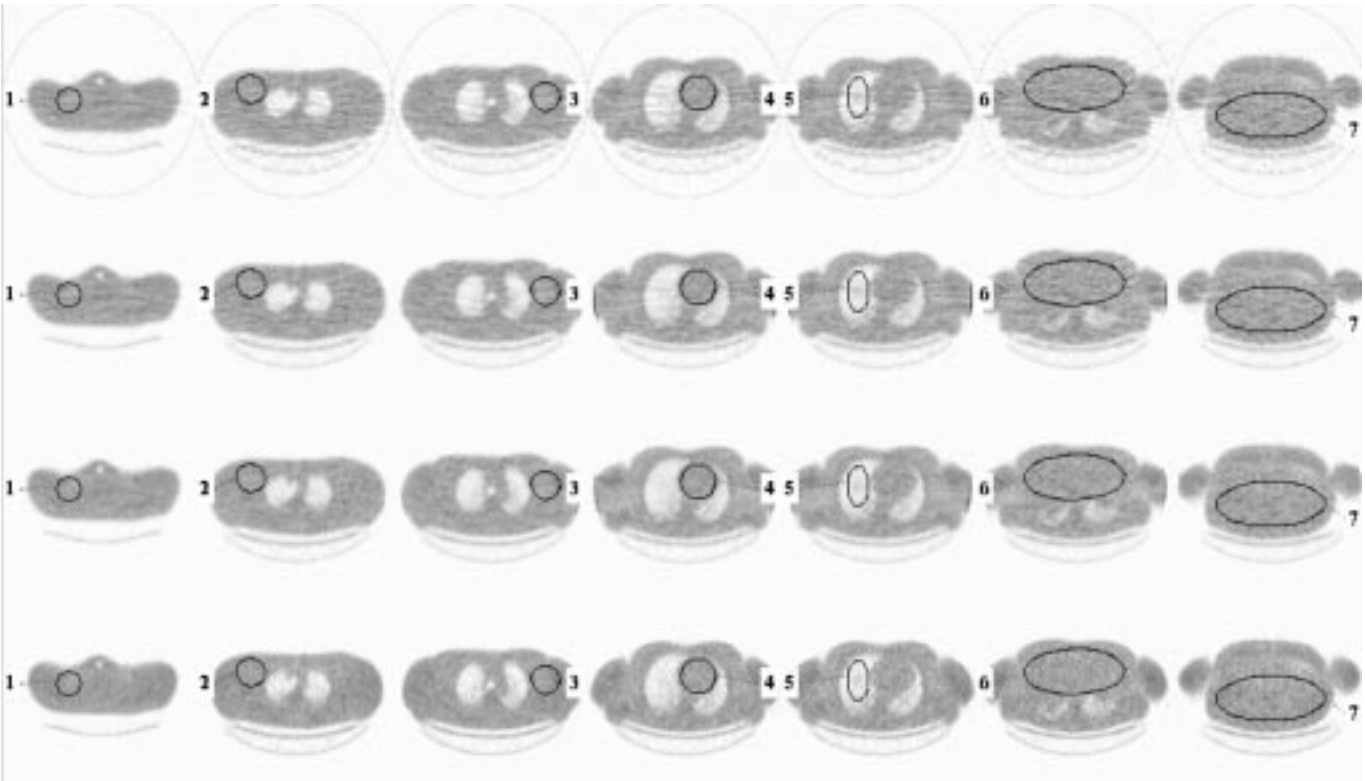

Fig. 10. Reconstruction images from the 10-min transmission scan. From top to bottom: FBP; UW ML-EM; NEC-scaled-ML-EM; and MLTR. For each algorithm, seven planes are shown with the seven regions in overlay.

the NEC-approach on the amount of uncorrelated noise, but unavoidably, NEC ML-EM suffers from "deterioration" at high iteration numbers, a well-known feature of ML-EM reconstruction from pure Poisson data [18]. The uncorrelated noise can

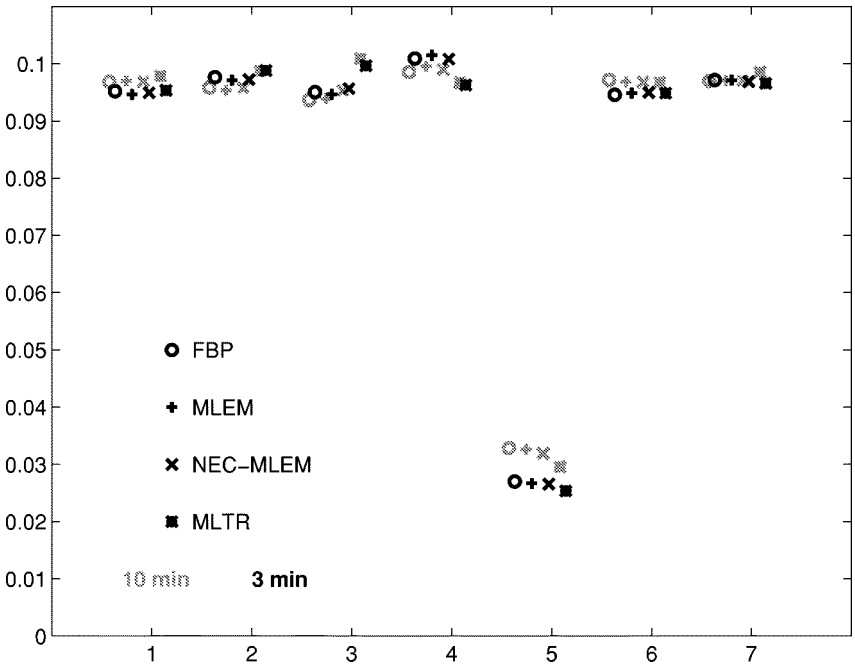

Fig. 11. Clinical transmission protocol: mean region-of-interest-values for the seven regions. Values from the 10-min image are in gray, values from the 3-min image are in black.

only be suppressed by increasing the precision of the data (e.g., by scanning longer) or by using additional information (implicitly by constraining, smoothing, stopping iterations early etc, or explicitly by incorporation of *a priori* probability distributions). The simulation of the contaminated emission scan nicely illustrates that NEC scaling reduces the correlated noise, and produces a reconstruction with a position-dependent point noise amplitude. The noise amplitude is higher in the region of the contamination, because this region is reconstructed from data with increased uncertainty.

The simulation of the contaminated emission sinogram confirms that NEC-shifted ML-EM converges slower than NEC-scaled-ML-EM, as expected from the update expressions (13) and (15). The step size is smallest in the region of contamination. As a result, that region is relatively homogeneous after 30 iterations and with 250 iterations, it is similar to the NEC-scaled ML-EM region at 30 iterations. Because the rate of convergence is dependent on position, it is difficult to compare images at low iteration numbers. When noise is suppressed by stopping iterations early, this position-dependent behavior can be advantageous. If noise is suppressed with priors, the faster convergence of NEC-scaled ML-EM seems preferable. The performance differences between the two methods decrease with decreasing contamination count.

The simulations show that the NEC-approach not only suppresses streak artifacts, it also increases the likelihood value. However, it is not obvious that this theoretical improvement also yields improvement in image quality for every application. The impact on clinical applications remains to be studied.

In the clinical transmission study, only the effect of the logarithmic transformation was included, assuming that the transmission scan was Poisson distributed. It is not, since for practical reasons, it has been precorrected for random coincidences and detection sensitivity variations (2-D-normalization), and it has been smoothed. The MLTR procedure used a more accurate model: it only ignored randoms precorrection, but took into account effects due to 2-D-normalization and dead time, and did not apply any pre-smoothing. Figs. 9 and 10 show that the NEC-scaled ML-EM reconstruction is similar to the MLTR reconstruction, suggesting that the precorrections have no dramatic effect on the noise characteristics.

The log conversion is a nonlinear operator and its application to noisy transmission data introduces positive bias. Since this bias is already present in the processed transmission sinogram, virtually any reconstruction algorithm applied to such a sinogram will produce a biased reconstruction. Presmoothing the blank and transmission scans reduces the noise and therefore also the bias. The quantitative analysis of the clinical experiment shows that presmoothing with a Gaussian mask of 8-mm FWHM was sufficient to reduce the differences in bias below the noise level.

We observed that convergence tends to slow down in highly attenuated regions, when a more accurate noise model is used. This can be seen by comparing the reconstruction of the arms in Figs. 9 and 10: the boundaries of the arms are better resolved in the FBP and UW ML-EM images than in the MLTR and NEC-scaled ML-EM images. So even though the likelihood may be higher, resolution and recovery may still lag behind in certain regions.

VI. Conclusion

The new method extends the ML-EM algorithm for emission tomography to a general purpose reconstruction algorithm. Since the method is based on very simple operations, existing implementations of the ML-EM algorithm, possibly accelerated with ordered subsets or other methods, can be used with minor or even without modification.

ACKNOWLEDGMENT

The authors would like to thank the anonymous reviewers for their valuable suggestions.

REFERENCES

[1] K. Lange and R. Carson, "EM reconstruction algorithms for emission and transmission tomography," *J. Comput. Assist. Tomogr.*, vol. 8, pp. 306–316, 1984.

[2] L. S. Shepp and Y. Vardi, "Maximum-likelihood reconstruction for emission tomography," *IEEE Trans. Med. Imag.*, vol. MI-1, pp. 113–122, 1982.

[3] D. G. Politte and D. L. Snyder, "Corrections for accidental coincidences and attenuation in maximum-likelihood image reconstruction for positron-emission tomography," *IEEE Trans. Med. Imag.*, vol. 10, pp. 82–89, Mar. 1991.

[4] M. Yavuz and J. A. Fessler, "Statistical image reconstruction methods for randoms-precorrected PET scans," *Med. Image Anal.*, vol. 2, pp. 369–378, 1997.

[5] J. A. Fessler, E. P. Ficaro, N. H. Clinthorne, and K. Lange, "Grouped-coordinate ascent algorithms for penalized-likelihood transmission image reconstruction," *IEEE Trans. Med. Imag.*, vol. 16, pp. 166–175, Apr. 1997.

[6] J. Nuyts, B. De Man, P. Dupont, M. Defrise, P. Suetens, and L. Mortelmans, "Iterative reconstruction for helical CT: A simulation study," *Phys. Med. Biol.*, vol. 43, pp. 729–737, 1998.

[7] M. H. Hudson and R. S. Larkin, "Accelerated image reconstruction using ordered subsets of projection data," *IEEE Trans. Med. Imag.*, vol. 13, pp. 601–609, Dec. 1994.

[8] C. Michel, M. Sibomana, A. Bol, X. Bernard, M. Defrise, C. Comtat, P. E. Kinahan, and D. Townsend, "Preserving Poisson characteristics of PET data with weighted OSEM reconstruction," in *Conf. Rec. IEEE NSS-MIC*, 1998, Paper M8-61.

[9] J. Nuyts, P. Dupont, S. Stroobants, A. Maes, L. Mortelmans, and P. Suetens, "Evaluation of maximum-likelihood based attenuation correction in positron emission tomography," *IEEE Trans. Nucl. Sci.*, vol. 46, pp. 1136–1141, Aug. 1999.

[10] S. C. Strother, M. E. Casey, and E. J. Hoffman, "Measuring PET scanner sensitivity: Relating count rates to image signal-to-noise ratios using noise-equivalent counts," *IEEE Trans. Nucl. Sci.*, vol. 37, pp. 783–788, Apr. 1990.

[11] J. A. Fessler, "Penalized weighted least-squares image reconstruction for positron emission tomography," *IEEE Trans. Med. Imag.*, vol. 13, pp. 290–300, 1994.

[12] R. Lewitt and G. Muehllehner, "Accelerated iterative reconstruction for positron emission tomography based on the EM algorithm for maximum likelihood estimation," *IEEE Trans. Med. Imag.*, vol. MI-5, pp. 16–22, 1986.

[13] W. H. Press, B. P. Flannery, S. A. Teukolsky, and W. T. Vetterling, *Numerical Recipes*. Cambridge, U.K.: Cambridge Univ.y Press, 1980, sec. 7.3.

[14] J. Nuyts, P. Dupont, and L. Mortelmans, "Iterative reconstruction of transmission sinograms with low signal to noise ratio," in *Proc. 2nd IEEE Workshop (1996) Computer Intensive Methods in Control and Signal Processing ("Can we beat the curse of dimensionality?")*, K. Warwick and M. Karny, Eds., Prague, Czech Republic, 1997, pp. 237–248.

[15] K. Wienhard, M. Dahlbom, L. Eriksson, C. Michel, T. Bruckbauer, U. Pietrzyk, and W. D. Heiss, "The ECAT EXACT HR: Performance of a new high-resolution positron scanner," *J. Comput. Assist. Tomogr.*, vol. 18, pp. 110–118, 1994.

[16] W. F. Jones, W. M. Digby, W. K. Luk, M. E. Casey, and L. G. Byars, "Optimizing rod window width in positron emission tomography," *IEEE Trans. Med. Imag.*, vol. 14, pp. 266–270, June 1995.

[17] M. Lonneux, T. Borbath, A. Bol, A. Coppens, M. Sibomana, R. Bausart, M. Defrise, S. Pauwels, and C. Michel, "Attenuation correction in whole-body FDG oncological studies: The role of statistical reconstruction," *Eur. J. Nucl. Med.*, vol. 26, pp. 591–598, 1999.

[18] E. Veklerov and J. Llacer, "Stopping rule for the MLE algorithm based on statistical hypothesis testing," *IEEE Trans. Med. Imag.*, vol. MI-6, pp. 313–319, 1987.